nature communications

Article

https://doi.org/10.1038/s41467-024-54083-7

Organic–inorganic covalent–ionic network enabled all–in–one multifunctional coating for flexible displays

Received: 27 June 2024

Accepted: 31 October 2024

Published online: 08 November 2024

Check for updates

Xiong Lin[1], Chen–Yu Li[1], Lu–Xuan Liang[1], Qing–Yun Guo[2], Yongzheng Zhang[1], Si–Rui Fu[1], Qin Zhang[1], Feng Chen[1], Di Han[1] ✉ & Qiang Fu[1] ✉

Touch displays are ubiquitous in modern technologies. However, current protective methods for emerging flexible displays against static, scratches, bending, and smudge rely on multilayer materials that impede progress towards flexible, lightweight, and multifunctional designs. Developing a single coating layer integrating all these functions remains challenging yet highly anticipated. Herein, we introduce an organic–inorganic covalent–ionic hybrid network that leverages the reorganizing interaction between siloxanes (i.e., trifluoropropyl–funtionalized polyhedral oligomeric silsesquioxane and cyclotrisiloxane) and fluoride ions. This nanoscale organic–inorganic covalent–ionic hybridized crosslinked network, combined with a low surface energy trifluoropropyl group, offers a monolithic layer coating with excellent optical, antistatic, anti–smudge properties, flexibility, scratch resistance, and recyclability. Compared with existing protective materials, this all–in–one coating demonstrates comprehensive multifunctionality and closed–loop recyclability, making it ideal for future flexible displays and contributing to ecological sustainability in consumer electronics.

Touch display, serving as a direct interface for human–machine interaction, has been widely adopted in consumer electronics (e.g., smartphone and tablets), medical devices, military equipment, and holds great potential in emerging fields such as virtual reality and the internet of things[1–5]. To ensure clear image display and accurate touch recognition, the protective cover window for touch displays must possess high transmittance, and suitable surface resistivity (10^6 ~ 10^{12} ohm sq^{-1}), to prevent static electricity accumulation on the surface and resulting electrostatic discharge and electrical malfunction when the surface resistance exceeds 10^{12} ohm sq^{-1}, as well as disabled capacitive touch recognition when the surface resistance falls below 10^6 ohm sq^{-1}[6–8]. Meanwhile, protective cover windows with extra excellent scratch resistance (i.e. high hardness), high flexibility, and anti-smudge properties are highly preferred for emerging flexible displays[9–11]. Currently, the prevailing approach employed by electronics companies or academic organizations involves individually depositing multiple layers (e.g., flexible substrate, flexible yet hard, antistatic, and anti-smudge layer) as cover windows to achieve the desired multiple functions (Fig. 1a). However, this results in complex fabrication procedures and intricate electronics structures, which significantly impede the trend toward lighter, thinner, and multifunctional designs for flexible touch displays. To overcome such limitations, integrating all these functions into a single coating layer is highly anticipated.

To achieve a coating layer that possesses all the required functions, several challenges must be overcome. One prominent obstacle is endowing a material with high transparency and antistatic properties, while the other challenge is imbuing it with ceramic-like scratch resistance and polymer–like compliance, which are typically mutually exclusive. Currently, the incorporation of conductive additives such as

[1]College of Polymer Science & Engineering, State Key Laboratory of Polymer Materials Engineering, Sichuan University, Chengdu, P. R. China. [2]Center for Advanced Low–Dimension Materials, State Key Laboratory for Modification of Chemical Fibers and Polymer Materials, College of Material Science and Engineering, Donghua University, Shanghai, P. R. China. ✉e-mail: handi@scu.edu.cn; qiangfu@scu.edu.cn

https://doi.org/10.1038/s41467-024-54083-7

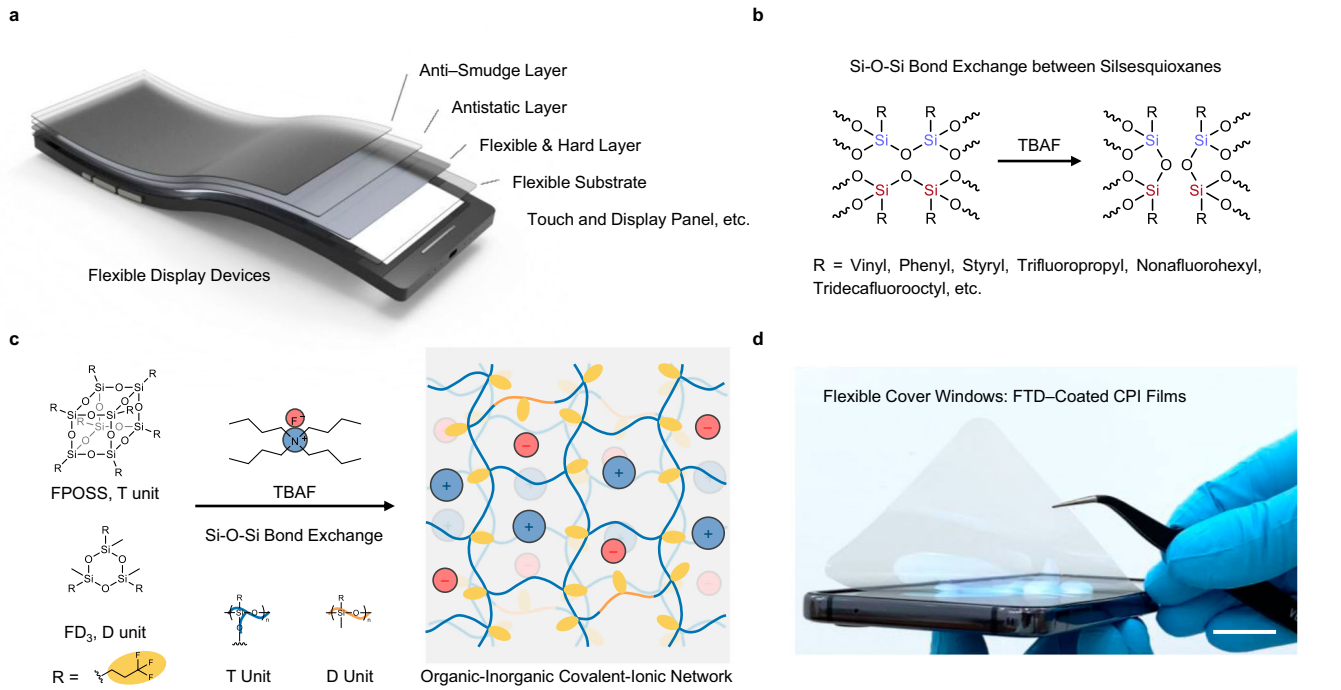

Fig. 1 | Design and fabrication of FTD coating. a Illustration of the structure of flexible display devices, the flexible cover windows include flexible substrate, flexible and hard layer, antistatic layer, and anti-smudge layer. **b** Reorganizing interaction mechanism between fluoride ions (derived from TBAF) and siloxanes. **c** Chemical structures of materials used for fabricating FTD coating and formation of organic–inorganic covalent–ionic networks. **d** Photograph of flexible cover windows comprising FTD–coated CPI films. Scale bar, 2 cm.

carbon nanotubes[12,13], metal nanowires[14], metal grids[15], and ionic salts[16,17] to polymers has been proved to be effective in achieving suitable surface resistivity. However, their incorporation often results in a loss of transparency due to factors such as the inherent color and poor dispersion of a large amount of conductive fillers[18,19]. More importantly, this leads to an inadequate balance between hardness and flexibility caused by modulus mismatching and the distinction of crack tips between the hard and soft components in the resulting hybrids[10,20]. Recently, there have been successful endeavors to demonstrate the promising potential of molecular-level hybridization between organics and inorganics for the fabrication of a single material possessing high transparency, hardness, and flexibility. Specifically, polysiloxanes with hyperbranched[21–23], ladder-like[10,24], and cage-like[11,25–27] architectures have emerged as the preferred choice for preparing flexible yet hard transparent coatings. The ingenious incorporation of functional groups could endow such coatings with extra anti-smudge[11,21,22,25,28], antibacterial[21,25], or self–healing[27,29] abilities. Nevertheless, achieving molecular-level hybridization with conductive components remains largely unexplored, it is still an urgent task to develop an all–in–one methodology that integrates multifunctionalities based on a simple and scalable strategy.

In this study, we develop a nanoscale organic–inorganic covalent–ionic hybrid network comprising trifluoropropyl–functionalized polyhedral oligomeric silsesquioxane (FPOSS, T units donor), 1,3,5–tris[(3,3,3–trifluoropropyl) methyl] cyclotrisiloxane (FD_3, D units donor), and tetrabutylammonium fluoride (TBAF) by exploiting the reorganizing interaction between fluoride ions (derived from TBAF) and siloxanes (Fig. 1b,c). This approach allows us to achieve what we term as trifluoropropyl–functionalized T and D units–based (FTD) coating materials. Adequate free ions (fluoride and tetrabutylammonium ions) allow the adjustment of the surface resistivity, while the crosslinked nanoscale organic–inorganic covalent–ionic hybrid networks and low surface energy groups (i.e., $-(CH_2)_2CF_3$) ensure their excellent optical, antistatic, mechanical, and anti-smudge properties without compromising each other. By depositing this all–in–one coating on flexible substrates such as colorless polyimide (CPI) films, the bilayered cover windows (Fig. 1d) exhibit an effective combination of excellent optical transparency, polymer–like flexibility, ceramic-like scratch resistance, anti-reflection, antistatic, anti-smudge properties in practical applications. More importantly, taking advantage of the reorganization between fluoride ions and siloxanes, this coating can be easily chemically recycled and reused on CPI films without scarificing their integral properties. This methodology not only promotes the development of lightweight, thin, and multifunctional consumer electronics but also enhances ecological sustainability.

Results

Materials design and fabrication

The interaction between fluoride ions and polyhedral oligomeric silsesquioxanes (POSSs) has proven to be a useful method for constructing ionic hybrid molecules through reorganization[30–33]. Thus, we envision that the incorporation of free fluoride and tetrabutylammonium ions will not only allow us to introduce adequate free ions at the molecular level for tuning surface resistivity[34] but will also facilitate the design of recyclable siloxane–based materials. Along with the presence of low surface energy groups[35–38] (e.g. trifluoropropyl), remarkable anti-smudge properties could be also achieved. In general, POSS salts encapsulated with fluoride ions are fabricated (Supplementary Fig. 1a,b)[30,31] due to the host–guest interaction between POSS cages containing electron-withdrawing substituents and fluoride ions. We propose that if certain components hinder the host–guest interaction between POSS cages with electron-withdrawing substituents and fluoride ions, crosslinked organic–inorganic covalent–ionic hybrid networks will be obtained. In our design, we selected cyclic siloxanes (i.e., D units), which possess distinct symmetry compared to POSS

https://doi.org/10.1038/s41467-024-54083-7

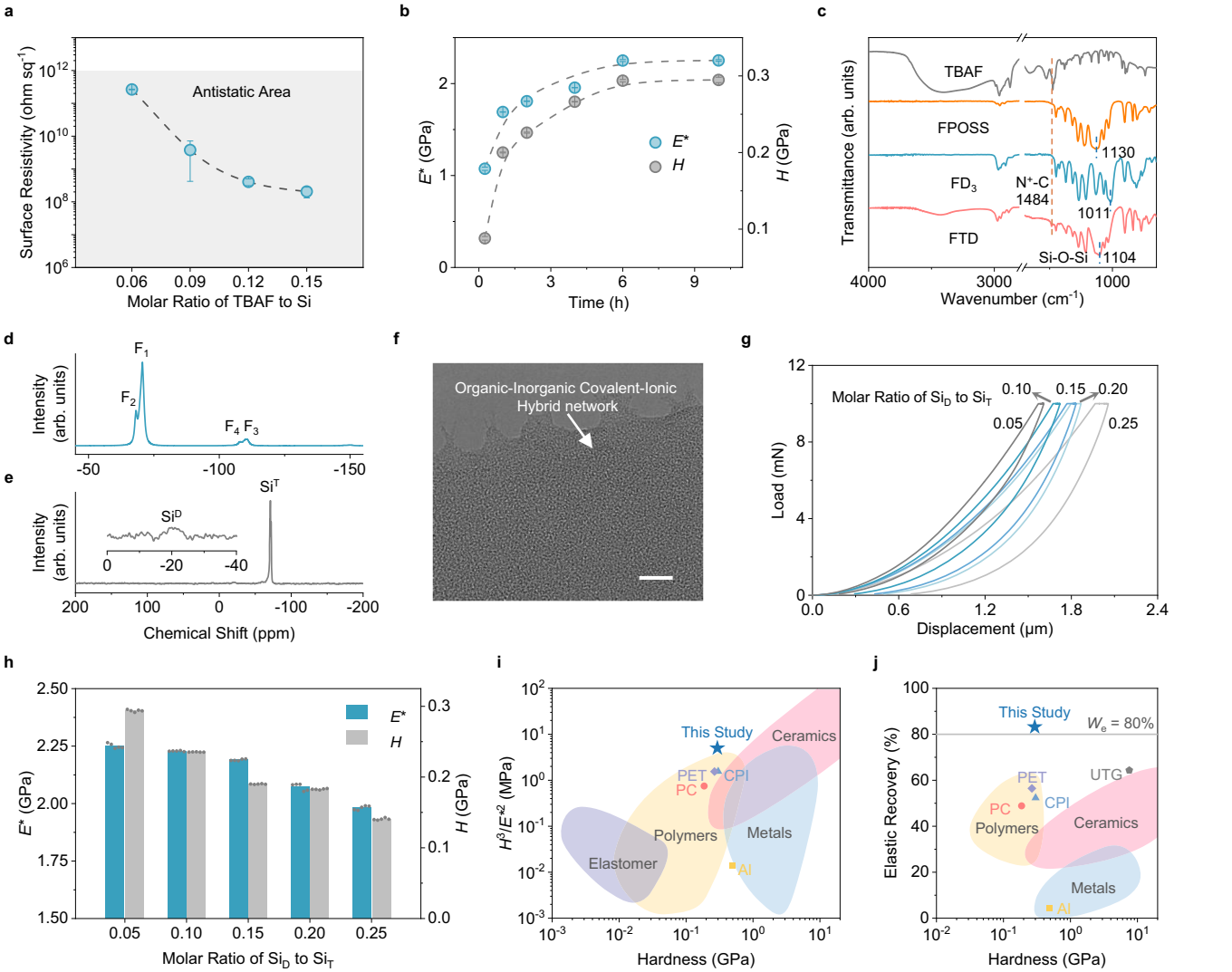

Fig. 2 | Properties characterization of FTD coatings. a Surface resistivities of samples with molar ratio of TBAF to Si ranging from 0.06 to 0.15. Error bars represent standard deviation, $n = 3$. **b** E^* and H of samples with different curing times. Error bars represent standard deviation, $n = 5$. **c** FT–IR spectra of TBAF, FPOSS, FD_3, and FTD coating. **d**–**f** ^{19}F CP–MAS NMR (**d**), ^{29}Si CP–MAS NMR spectra (**e**), and a TEM image (**f**) of the FTD coating. Scale bar, 10 nm. **g**,**h** Representative load–displacement curves (**g**) and E^* and H (**h**) of samples with molar ratio of Si_D to Si_T ranging from 0.05 to 0.25. Individual measurements are represented by gray dots, and the average of the five measurements is given. **i** Comparison of H^3/E^{*2} versus H for Al, PC, CPI, PET, FTD coating and other typical engineering materials, including ceramics, metals, elastomer, and polymers. Reproduced with permission[44]. Copyright 2023, Springer Nature. **j** Comparison of elastic recovery versus H for Al, PC, CPI, PET, UTG, FTD coating and other typical engineering materials, including ceramics, metals, and polymers. The area above the gray line represents a region where $W_e \geq 80\%$. Reproduced with permission[44]. Copyright 2023, Springer Nature. Source data are provided as a Source Data file.

(i.e., T units) and can be reorganized by fluoride ions[39,40], to hinder the host–guest interaction between POSS cages and fluoride ions (Supplementary Fig. 1a,c). By combining this with FPOSS matrix and TBAF, a highly crosslinked organic–inorganic covalent–ionic hybrid networks–based material is developed (Fig. 1b,c). Typically, the incorporation of FD_3 leads to the formation of a transparent coating rather than an opaque one (Supplementary Fig. 2).

After obtaining the material, we started to evaluate the influence of ions content on the morphology and surface resistivity of organic–inorganic covalent–ionic hybrid networks. As seen from the scanning electron microscopy (SEM) images of samples with insufficient ions (molar ratio of TBAF to Si = 0.03), they are brittle and there are obvious cracks on the surface after fully curing procedure (Supplementary Fig. 3a). With higher content of ions (molar ratio of TBAF to Si > 0.03), smooth morphology could be obtained (Supplementary Fig. 3b, c), but for samples with excessive ions (molar ratio of TBAF to Si = 0.15), fluoride and tetrabutylammonium ions tend to aggregate in the form of ionic salts and destroy the smoothness of the surface (Supplementary Fig. 3d,e). Therefore, suitable content of ions (molar ratio of TBAF to Si > 0.03 and <0.15) were identified to be important to achieve a smooth surface morphology and amorphous networks. Furthermore, surface resistivity results (Fig. 2a) show that surface resistivities are decreased with increasing ions content, reaching the common antistatic range (10^6 ~ 10^{12} ohm sq^{-1}). Consequently, to ensure both a smooth surface and low surface resistivity (~ 4×10^8 ohm sq^{-1}), a molar ratio of TBAF to Si of 0.12 was selected for materials fabrication. Following the determination of ions content, the optimal curing time was evaluated based on mechanical properties. As shown in load–displacement curves (Supplementary Fig. 4), the smaller hysteresis arises at samples with longer curing time, and their corresponding effective modulus (E^*) and hardness (H) increase to a stable value, suggesting an optimal curing time of 6 h (Fig. 2b). And the rheological

properties of the FTD coating (Supplementary Fig. 5) are recorded to illustrate the network formation. Firstly, siloxanes with T and D structures reorganize in a solvent with the catalysis of fluoride ions due to the dynamic nature of the Si–O–Si bond under this condition. Then the fragmentized siloxanes reorganize and form abundant Si–O–Si bond to gradually construct crosslinked networks during the solution volatilization. As most of the solutions volatilized, the storage modulus (G') and loss modulus (G'') reach a plateau, reflecting the thermodynamic equilibrium of solution volatilization. At higher temperature and lower pressure (50 °C under vacuum), further volatilization of the residual solution results in a highly crosslinked Si–O–Si crosslinked network, providing a robust framework for achieving high hardness. After 6 h at 50 °C under vacuum, the G' and G'' of FTD coating approach constant values like modulus and hardness, indicating that optimized FTD coating has been achieved.

The interactions between hybrid siloxanes and ions in the FTD coating were analyzed by Fourier transform infrared (FTIR), ^{19}F, and ^{29}Si cross–polarization/magic–angle spinning (CP–MAS) NMR spectroscopy. The FTIR spectrum of FTD coating exhibit the combination of Si–O–Si vibration of FPOSS at 1130 cm^{-1} and N^+–C vibration of TBAF at 1484 cm^{-1}, as well as the disappearance of Si–O–Si vibration of strained cyclic FD_3 at 1011 cm^{-1}, indicating the successful preparation of the FTD coating (Fig. 2c and Supplementary Fig. 6). Meanwhile, the vibration of Si–O–Si in FPOSS is redshifted to 1104 cm^{-1} in the FTD coating. These shifts in the FT–IR spectra suggest the formation of ionic interactions between hybrid siloxanes and fluoride and tetrabutylammonium ions. The ^{19}F CP–MAS NMR spectra further confirm these interactions, according to the shift of the $-(CH_2)_2CF_3$ peak from −69.4 ppm in both FPOSS and FD_3 to −70.6 (F_1, for $-CF_3$ on FPOSS) and −68.2 (F_2, for $-CF_3$ on FD_3) ppm in the FTD coating, and shift of fluoride ions peak from −113.8 ppm to −110.4 (F_3, for free fluoride ions) and −108.0 (F_4, for a small amount of F–Si bond) ppm in the FTD coating (Fig. 2d and Supplementary Fig. 7a). Furthermore, the ^{29}Si CP–MAS NMR spectra confirm the presence of two Si types, Si^T and Si^D[41,42], and reveal a shift of the Si^T peak from −69.8 ppm in FPOSS to −71.1 ppm in the FTD coating (Fig. 2e and Supplementary Fig. 7b). This shift is lower than the shift of approximately 3.7 ppm observed for the formation of FPOSS salts encapsulated with fluoride ions[31], indicating the construction of organic–inorganic covalent–ionic interactions in the hybrid networks of the FTD coating.

Moreover, the scale of interactions between hybrid siloxanes and ions in FTD coating was evaluated using transmission electron microscopy (TEM). The TEM image (Fig. 2f) of FTD coating shows the presence of amorphous hybrid networks at the nanometer scale. The energy–dispersive X-ray spectroscopy (EDS) results (Supplementary Fig. 8) indicate uniform dispersion of elements C, O, N, F, and Si in the FTD coating, with experimental relative elements contents close to theoretical values (Supplementary Table 1). Such uniformity on the nanoscale scale indicates the effective hybridization of organic–inorganic covalent–ionic networks, contributing to the high transmittance and the integration of flexibility and hardness of FTD coating.

Furthermore, beyond the significant role of FD_3 in fabricating transparent coating, we investigated the influence of FD_3 content on mechanical properties. Parameters including H^3/E^{*2}, and elastic recovery (W_e) were used to evaluate scratch resistance and resilience, respectively[43]. Firstly, the FD_3 content shows negligible influence on surface resistivities (Supplementary Fig. 9). However, coatings with higher FD_3 content exhibit larger hysteresis in load–displacement curves (Fig. 2g), with corresponding decreases in E^* and H of the coatings (Fig. 2h) from 2.25 and 0.29 GPa to 1.98 and 0.14 GPa, respectively, as the molar ratio of Si_D to Si_T increases from 0.05 to 0.25. Consequently, the FTD coating with the molar ratio Si_D to Si_T of 0.05 demonstrates the highest value of H^3/E^{*2} and elastic recovery (Supplementary Fig. 10), which are 5.01 MPa and 83.2%, respectively. SEM images (Supplementary Fig. 11) reveal a rough surface, indicating that further reduction in FD_3 content is not feasible as sufficient FD_3 is necessary to hinder the formation of POSS salts encapsulated with fluoride ions. Therefore, FTD coating with the molar ratio of Si_D to Si_T as 0.05 was chosen as the representative coating for practical applications. To evaluate the accuracy of nanoindentation measurement for FTD coating, different loads (10, 100, and 500 mN) are applied (Supplementary Fig. 12). The E^* and H of FTD coating remain more or less constant under different test loads. Compared with common materials (Supplementary Fig. 13), such as aluminum (Al), polycarbonate (PC), CPI, polyethylene terephthalate (PET) films, and ultrathin glass (UTG), as well as typical engineering materials like ceramics, metals, elastomer, and polymers[44], FTD coating exhibit excellent polymer–like flexibility (low E^*, 2.25 GPa), ceramic-like scratch resistance ($H^3/E^{*2} > 5$ MPa), and resilience ($W_e > 80\%$), highlighting its potential as a protective coating for flexible displays (Fig. 2i, j).

Electrostatic protection properties

To characterize the antistatic properties of the FTD coating, we designed two experiments to evaluate external and internal electrostatic protection properties, respectively. For the external electrostatic protection property, electroneutral samples are initially charged with positive or negative charges and ions by shots from an ion gun as seen in the illustration (Fig. 3a). Subsequently, the charged samples are transferred into a Faraday cup connected to an electrometer to record the decay of external electrostatic charges. Specifically, we compared the external electrostatic protection property of the FTD coating with UTG, PET and CPI. In comparison, the accumulated charges dissipate below 50% within a few minutes for the FTD coating, regardless of the type of charges, whereas the charges remain higher than 50% for UTG, PET, and CPI even after 30 min, indicating the excellent antistatic properties of FTD coating (Fig. 3b).

We further examined the internal electrostatic protection property by evaluating changes in surface potential before and after triboelectric charging with a copper rod. Contact potential differences (V_{CPD}) recorded via Kelvin probe force microscopy (KPFM) are used to derive the surface potential of samples, and the change in V_{CPD} (i.e., ΔV_{CPD}) reflects triboelectric properties such as charge transfer direction and charging ability. We compared the triboelectric properties of the FTD coating with common flexible materials, including UTG, PET, CPI, and commercial touch display cover windows (AF–UTG, commercial anti–fingerprint molecules treated UTG) (Fig. 3c, d). The V_{CPD} images show that after only five abrasions with a copper rod, the corresponding V_{CPD} values for UTG, PET, CPI, and AF–UTG change significantly, with ΔV_{CPD} values following the triboelectric series (Fig. 3e, f). In contrast, the values of V_{CPD} for the FTD coating remain unchanged even after 200 times continuous abrasions, and the ΔV_{CPD} value for the FTD coating is 25 ~ 80 orders of magnitude smaller than that of the common substrates, indicating excellent antistatic properties of the FTD coating. This is attributed to fast charge dissipation during the triboelectric charging process, resulted from effective nanoscale hybridization of organic–inorganic covalent–ionic networks.

Multifunctionality

We selected CPI films as flexible substrates to further investigate the properties of the FTD coating as flexible cover windows in practical applications. Due to the uniform organic–inorganic covalent–ionic hybrid networks on the nanometer scale, the FTD coatings possesses high transmittance (Fig. 4a) in the visible spectrum (99.6% at 550 nm), leading to highly transparent flexible cover windows (FTD–coated CPI films, Fig. 4b). Atomic force microscope (AFM) images indicate a smooth surface for the FTD coating with a roughness R_a of 0.99 nm, showing no obvious phase separation or aggregation (Supplementary Fig. 14). Additionally, due to the lower reflectance (Supplementary

https://doi.org/10.1038/s41467-024-54083-7

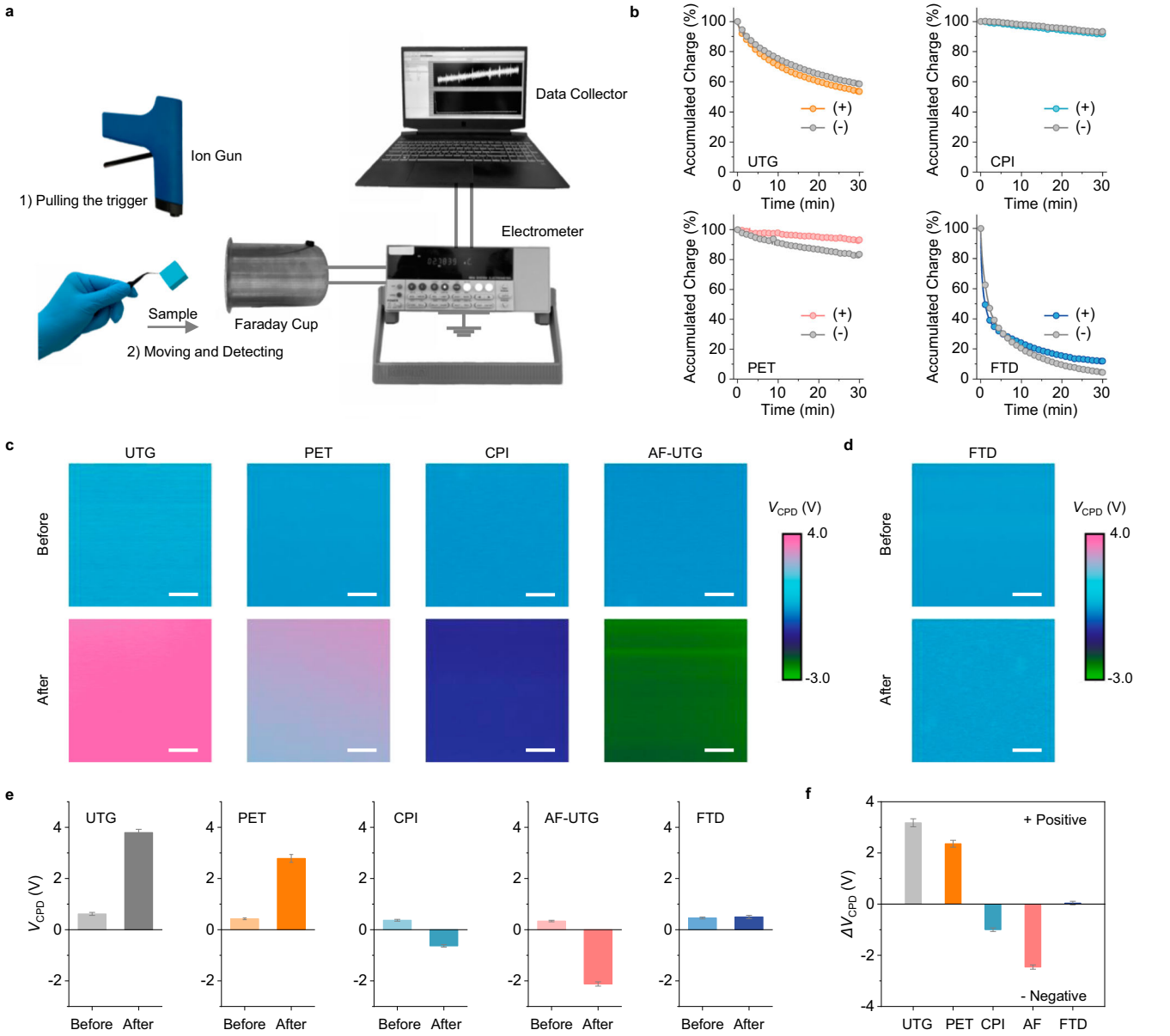

Fig. 3 | External and internal static protection properties. a Illustration of external electrostatic charges dissipation apparatus. **b** External electrostatic charges decay curves of UTG, CPI, PET, and FTD coating in this work. **c** KPFM images of UTG, PET, CPI, and AF–UTG before and after 5 times abrasion of copper rod. Scale bars, 2 μm. **d** KPFM images of FTD coating before and after 200 times abrasion of copper rod. Scale bars, 2 μm. **e**,**f** Comparison of the measured contact potential differences on various surfaces before and after friction (**e**) and their corresponding change (**f**). Error bars represent standard deviation and are calculated from the values of KPFM images. Source data are provided as a Source Data file.

Fig. 15a) and refractive index compared to CPI films (FTD coating, ~1.45; CPI, ~1.59, at 550 nm, Supplementary Fig. 15b), the FTD coating exhibit excellent anti-reflection properties for CPI films, resulting in higher transmittance of bilayered cover windows than original CPI films (Fig. 4a, b) in the visible spectrum (400–800 nm). Subsequently, water and oil (diiodomethane) are used to evaluate the anti-smudge properties of the FTD coating compared to UTG, PET, and CPI (Fig. 4c). Among them, the FTD coating exhibit the highest water and oil contact angle (107.3° and 76.2°, respectively) and low surface energy (19.5 mN m^{-1}) due to its abundant trifluoropropyl groups (–$(CH_2)_2CF_3$, low surface energy group), contributing to excellent anti-smudge ability (Fig. 4d and Supplementary Movie 1) and low adhesion during scratch.

As a robust and flexible protective coating, FTD–coated CPI films could withstand scratches from standard pencil exceeding 7H (Supplementary Fig. 16), much higher than CPI (2B) and PET (6B) films, and close to the pencil hardness of UTG (9H). We further examined the scratch resistance of the FTD coating using the steel wool wear test. A pressure of ~ 50 kPa (500 g on an area of 1 cm^2) is applied using fresh steel wool wrapped on a tester on the practical touch display carrying the FTD–coating (Fig. 4e). SEM images (Fig. 4f) show obvious scratches on the CPI films after only 30 abrasions, while no obvious scratches are observed on the FTD–coated CPI films even after 2500 abrasions. Meanwhile, the water and oil contact angles and surface resistivity for areas with different abrasion times remain similar to the original ones (Fig. 4g), indicating the excellent scratch resistance of the FTD coating. Additionally, the friction coefficient of the FTD coating (~0.09), measured by the nano-scratch test (Fig. 4h), is much lower than that of CPI and PET, even UTG and AF–UTG. This is also an important factor contributing to the excellent scratch resistance of the FTD coating. We believed that the excellent scratch resistance and low coefficient of

https://doi.org/10.1038/s41467-024-54083-7

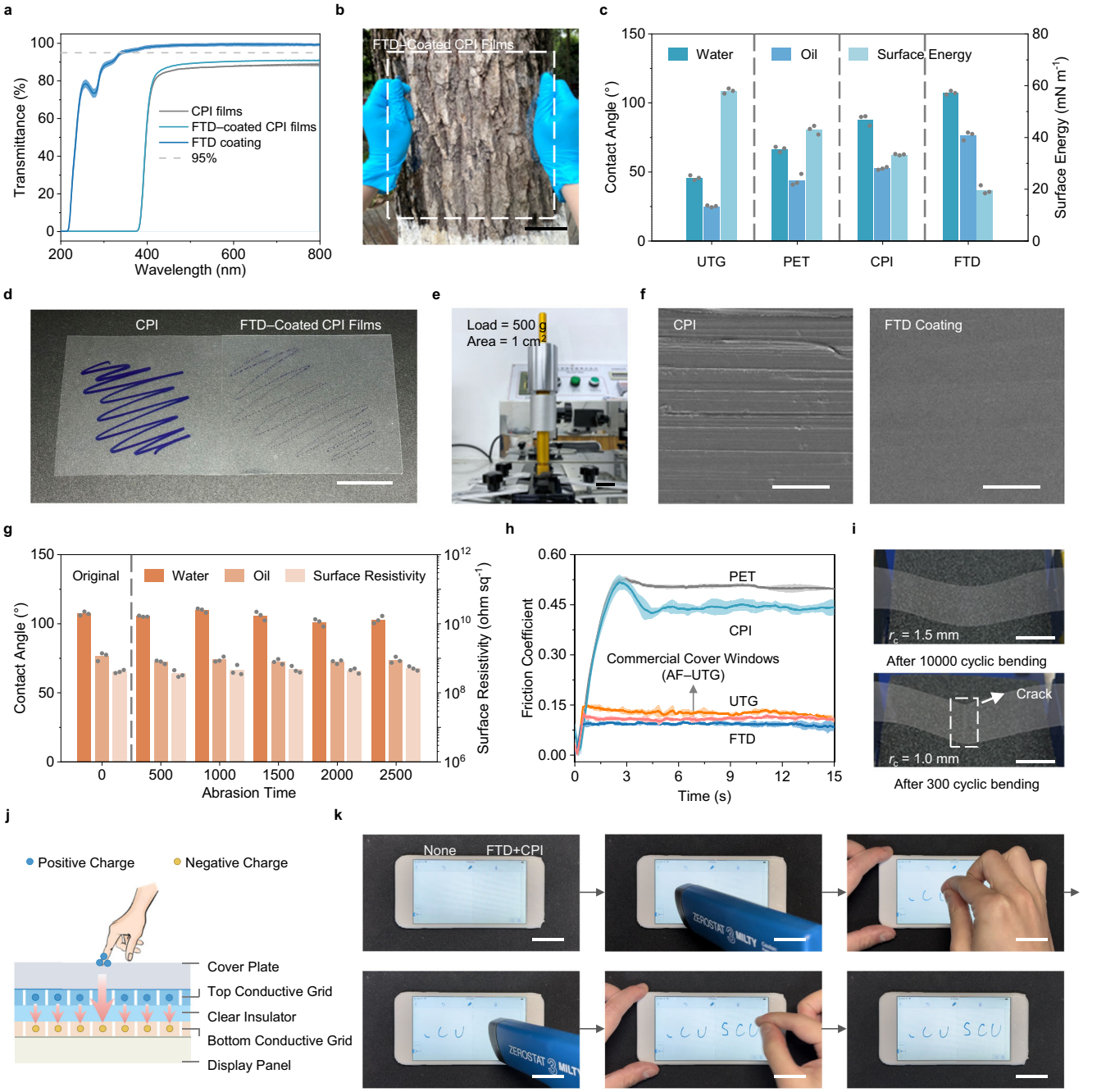

Fig. 4 | Multifunctionality of FTD coating materials. a Transmittance from 200 to 800 nm of FTD coating, CPI films, and FTD–coated CPI films. Error bars represent standard deviation, $n = 3$. **b** Photograph of large–scale flexible cover windows comprising FTD–coated CPI films. Scale bar, 5 cm. **c** Water and oil contact angles and surface energy of UTG, PET, CPI, and FTD coating. Individual measurements are represented by gray dots, and the average of the three measurements is given. **d** Anti-smudge ability of FTD–coated CPI films. Scale bar, 2 cm. **e** A photograph of the steel wool wear test apparatus. Scale bar, 2 cm. **f** SEM images of CPI films after 30 times abrasion and coating after 2500 times abrasion. Scale bars, 100 µm. **g** Water and oil contact angles and surface resistivity of coatings at different abrasion times. Individual measurements are represented by gray dots, and the average of the three measurements is given. **h** The friction coefficients of UTG, PET, CPI films, AF–UTG, and FTD coating that obtained from nano-scratch tests. Error bars represent standard deviation, $n = 3$. **i** Photographs of the flexibility tests conducted on FTD–coated CPI films. The images reveal no cracks in the bending areas even after undergoing over 10,000 cycles of bending when the r_c is set to 1.5 mm. However, when the r_c is reduced to 1.0 mm, cracks begin to appear after 300 cycles of bending. Scale bars, 2 cm. **j** Illustration of the capacitive touch control mechanism. **k** Touch control property of FTD–coated CPI films. Scale bars, 3 cm. Source data are provided as a Source Data file.

friction were attributed to tight crosslinked Si–O–Si networks, low surface energy (low adhesion during scratch), and low surface roughness. Furthermore, FTD–coated CPI films exhibit good flexibility attributed to the low E^* of the FTD coating (2.25 GPa). Such composite films could be freely bended into U–shape with a bending curvature radius (r_c) of 1.5 mm without generating cracks over 10,000 bending cycles (Fig. 4i, Supplementary Fig. 17, and Supplementary Movie 2). When the bending curvature radius is set to 1.0 mm, cracks are generated after 300 bending cycles. The adhesion performance of FTD coatings was tested by using the pull–off adhesion test. The adhesion strength of the FTD coating (0.81 ± 0.01 MPa) on the CPI films is attributed to the formation of chemical bonds between the Si–OH

https://doi.org/10.1038/s41467-024-54083-7

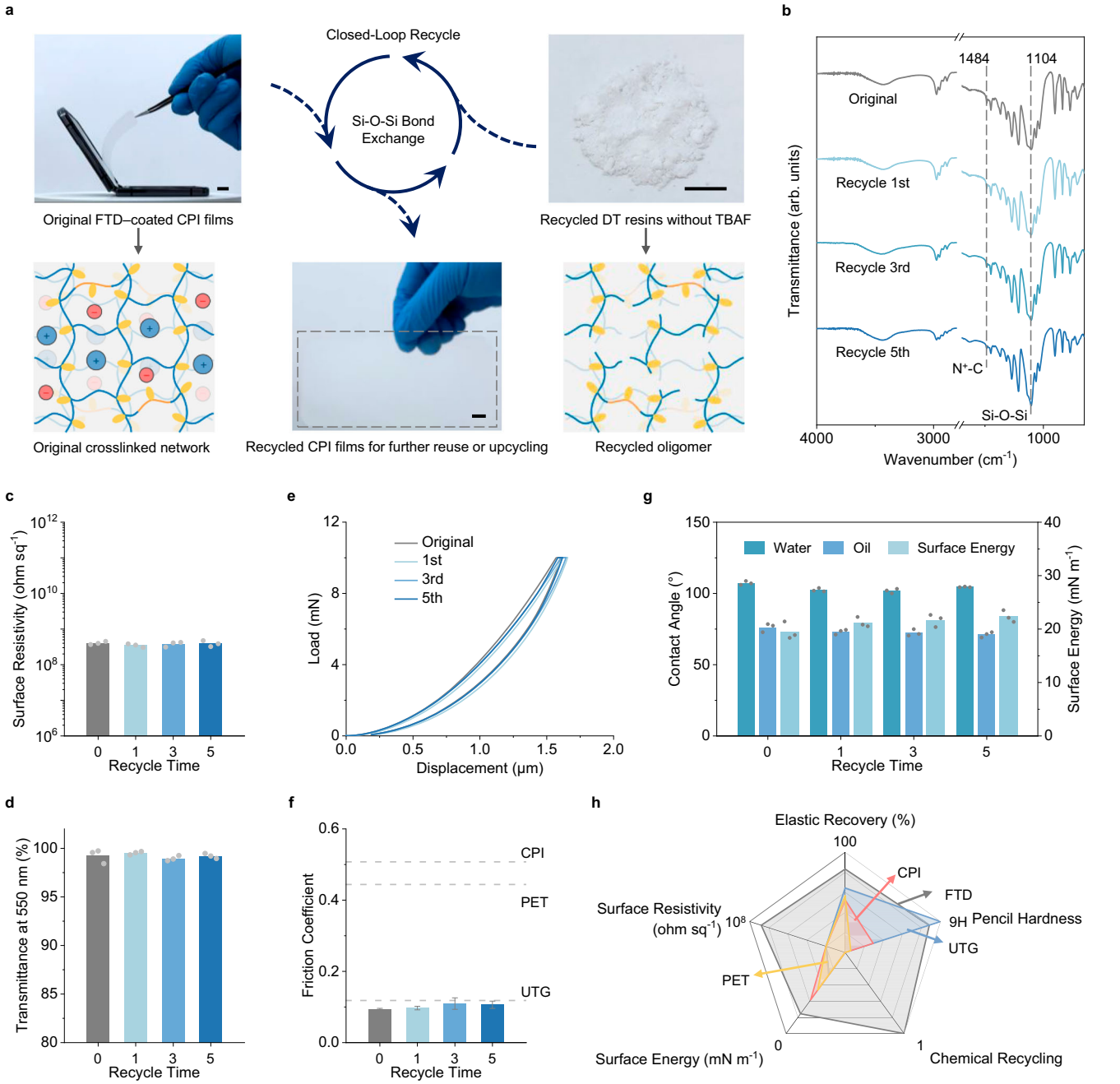

Fig. 5 | Closed-loop recycling of FTD coating materials. a Illustration of the chemical recycling of FTD coating. Scale bars, 1 cm. **b**–**g** FT–IR spectra (**b**), surface resistivity (**c**), transmittance at 550 nm (**d**), representative load–displacement curves (**e**), friction coefficient (**f**), and water and oil contact angle and surface energy (**g**) of recycled FTD coatings with different recycle times. Error bars (**f**) represent standard deviation, $n = 3$. Individual measurements (**c**) (**d**) (**g**) are represented by gray dots, and the averages of the three measurements are given. **h** Radar diagram comparison of the value of elastic recovery, pencil hardness, surface resistivity, surface energy, and chemical recyclability on commercial flexible cover substrate including UTG, CPI, and PET films, and FTD coating. Source data are provided as a Source Data file.

groups, generated during the siloxane reorganization, and the –OH groups on the polar CPI substrates, which are generated during the treatment with oxygen plasma. This strength is comparable to that of some previously reported coating materials on flexible substrates (Supplementary Table 2). Moreover, after alternant high temperature (80 °C) and ultraviolet light (27 mW cm^{-2}) for 14 days, the surface morphology, transmittance, surface resistivity, and pencil hardness of FTD–coated CPI films remain compared to the original ones (Supplementary Fig. 18), indicating its high photothermal stability for long–term photothermal environments.

More importantly, antistatic properties are crucial for protective cover windows for touch displays. As illustrated in the touch control diagram (Fig. 4j), touch signals rely on variations in surface charge density, which have significant influence on touch control precision. However, residual charges often remain after finger touches or contacts with pockets or packets. If these charges do not dissipate promptly, they can affect touch recognition accuracy, user experience, and even damage vital electronic components beneath the screen. To assess the practical applicability of the FTD coating in touch displays, we install a flexible cover window with half of its surface coated with

the FTD coating onto a touch panel eliminated an electrostatic module (Fig. 4k and Supplementary Movie 3). After some shots from the ion gun, we wrote the characters "SCU" on both cover windows, one with the FTD coating and the other without. Touch test results were evaluated based on the legibility of the written characters "SCU". Specifically, noticeable defects are observed on the side of the original CPI films, while the characters on the side of FTD–coated CPI films are intact, demonstrating excellent antistatic properties in practical touch displays.

Closed-loop recycling

The complexity of electronics significantly amplifies the challenge and expense associated with separating and recycling electronic waste (e-waste), resulting in a majority being directly disposed of in landfills and incinerators. This leads to ecological and environmental pollution, as well as a substantial wastage of resources[45–50]. Therefore, endowing such all–in–one coating with additional chemical recyclability holds immense value for fostering a sustainable future.

As depicted in the illustration (Fig. 5a and Supplementary Fig. 19), the closed-loop recycling of the FTD coating can be easily achieved due to its reversible organic–inorganic covalent–ionic hybrid networks. Using TBAF as the catalyst for the depolymerization and reorganization of organic–inorganic covalent–ionic hybrid networks, the FTD coating could be removed from the CPI films surface within 3 h. After removing the CPI films, the resulting solution is to be treated with calcium chloride ($CaCl_2$) to remove the fluoride ions. Subsequently, white powders obtained through rotary evaporating, washing, and vacuum drying are added to TBAF/tetrahydrofuran (THF) solution and used to fabricate FTD coating according to the original procedures. Evaluated by FT–IR (Fig. 5b and Supplementary Fig. 20), ^{29}Si CP–MAS NMR, ^{19}F CP–MAS NMR, and EDS spectra (Supplementary Figs. 21 and 22), the recycled FTD coatings exhibit consistent chemical structures and relative elements content compared to the original FTD coating even after five recycling cycles, indicating the preservation of the organic–inorganic covalent–ionic hybrid networks during recycling.

Beyond the composition and structures, we further characterized the electric, optical, mechanical, and surface properties of the recycled FTD coatings. Among them, the surface resistivity results (Fig. 5c) show that the recycled FTD coatings possess close surface resistivity (~ 4×10^8 ohm sq^{-1}) to the original FTD coating. This suggests that the excellent antistatic properties of the original FTD coating are maintained in recycled FTD coatings. Additionally, the recycled FTD coatings exhibit fully recovered high transmittance and anti-reflective properties for CPI films (Fig. 5d and Supplementary Fig. 23). Meanwhile, recycled FTD coatings exhibit similar load–displacement curves (Fig. 5e), indicating that they fully recover mechanical properties such as E^*, H, H^3/E^{*2}, and elastic recovery (Supplementary Fig. 24). Combined with consistent friction coefficients (Fig. 5f and Supplementary Fig. 25), the scratch resistance and flexibility of the recycled FTD coatings could be fully recovered. Moreover, they also exhibit fully recovered high water/oil contact angles and low surface energy (Fig. 5g), ensuring their anti-smudge properties.

The construction of organic–inorganic covalent–ionic hybrid networks combine high transmittance, excellent anti-smudge ability, scratch resistance, flexibility and, more importantly, antistatic properties for touch control, as well as degradable/recyclable properties, leading to the generation of an all–in–one coating for present flexible displays and future flexible electronics. The properties of such coating surpass those of current flexible cover windows (Fig. 5h). This work establishes the indispensable role of reorganization in the rational design of all–in–one multifunctional material, which may not only advance the development of consumer electronics towards lightweight and thin designs, but also promote ecological and environmental sustainability.

Discussion

In summary, we develop an organic–inorganic covalent–ionic hybrid network, which enables integration of the necessary multifunctionality into flexible display cover windows in a monolithic manner. The simultaneous integration of FTD coating with excellent optic, antistatic, anti-smudge properties, polymer–like flexibility, ceramic-like scratch resistance, and chemical recyclability, resulting from the nanoscale organic–inorganic covalent–ionic hybrid network holds tremendous potential for expanding the scope of flexible displays in next-generation flexible electronics. Specifically, we provide a reliable method to fabricate all–in–one solution for flexible display cover windows, while being comprehensive in comparison to existing flexible cover windows; such coating can be effectively chemical recycled and reused multiple times. As such, we anticipate that this methodology could present substantial opportunities for researchers seeking an extension of the functionality of protective coating, offering a facile tool to integrate multifunctionality into a monolithic layer.

Methods

Materials

FPOSS (cage mixture, Hybrid Plastics, FL0578), FD_3 (Adamas, 98 + %), THF (Greagent, 99.5 + %), $CaCl_2$ (Greagent, 97.0 + %), kieselguhr (200 mesh, Greagent, 89.0 + %), TBAF (1 M in THF, Adamas), CPI films (50 and 30 μm, Liaoning Oxiran Huahui New Material Co., LTD, China). THF utilized for reactions was dried through a solvent purification system (SPS – 5, Etelux, Beijing, China), and the other chemicals were used as received without further purification.

Preparation of the FTD materials

The title materials were fabricated as follows. Taking FTD as an example, FPOSS (1.0 g, 0.84 mmol) and FD_3 (0.05 g, 0.11 mmol) were dissolved in THF (5 mL) in a 10 mL vial with a magnetic stirring bar. Then, TBAF (0.84 mL, 1 M in THF) was added to the solution mixture and stirred at room temperature for 3 h. The resulting solution was bar-coated on substrate such as glass and CPI films, etc. after oxygen plasma treatment (400 W for 5 min) to increase the hydroxyl groups (–OH) on the surface of substrate. Each coating sample was first dried at room temperature under argon flow for 1 h and then cured at 50 °C under vacuum for 6 h. Other Samples with different contents of TBAF and FD_3 were prepared using the same procedures. The thickness of coating was adjusted by tuning the gap between the substrate and the bar. Unless otherwise specified, the thickness of the coating is 50 μm.

Recycling of the FTD materials

The FTD–coated films (FTD mass is ~1.0 g) were soaked in a THF solution with TBAF (0.1 M, 20 mL) for 3 h. After taking the films out, $CaCl_2$ (1.0 g) and a magnetic stirring bar were added to the resulting solution, and the solution mixture was stirred for 12 h to remove the fluoride ions and then filtered through kieselguhr. White solid (yield ~86%) was obtained by rotary evaporating the solvent, methanol washing (three times), and vacuum drying (80 °C for 12 h). To refabricate FTD coating, the resulting product (1.0 g) and TBAF (0.8 mL, 1 M in THF) were added to THF (4.8 mL) in a 10 mL vial with a magnetic stirring bar and stirred at room temperature for 3 h. The coating and curing procedures were identical to those used in the production of original FTD coating. Recycling of FTD coating with more recycling times was obtained from repeating the abovementioned procedures.

Size exclusion chromatography

Size exclusion chromatography (SEC) analyzes for samples were recorded using a Waters 1515 instrument (Waters, America) equipped with a gel column, a differential refractive index detector, and a light scattering detector. The eluent solvent, sample concentration, and flow rate were THF, 2 mg mL^{-1}, and 0.5 mL min^{-1}, respectively, with polystyrene utilized as the standard for molecular weight calculation.

Morphology and elements analysis
SEM images and EDS two-dimensional mappings of C, N, O, F, Si elements were acquired on a Nova NanoSEM450 SEM (FEI, America) with an X-MaxN EDS instrument (Oxford Instruments, England) at an operating voltage of 10 kV. Before SEM and/or EDS analysis, all samples were sputtered with a thin layer of gold to reduce the charging effect. TEM images and the corresponding EDS mapping of C, N, O, F, and Si elements were captured on a Talos F200i microscope (Thermo Fisher Scientific, America) operating at 200 kV.

Surface resistivity
Surface resistivity results were obtained using a two-probe method under ambient conditions (room temperature, ~25 °C; relative humidity, ~40%) on a 6514B electrometer (Keithley, America).

Wide angle X-ray diffraction
Wide angle X-ray diffraction (WAXD) patterns were recorded on an X'pert pro MPD X-ray diffractometer (PANalytical B.V., Netherlands) with Cu Kα radiation ($\lambda = 1.5406$ Å) at an operating voltage of 40 kV and current of 40 mA. The diffraction angle (2θ) range was 2–90° with a scan speed of 10° min^{-1}.

Nanoindentation
Nanoindentation analysis was performed under ambient conditions (room temperature, ~25 °C; relative humidity, ~40%) on a TI 980 nanoindenter (Bruker, USA) equipped with a diamond Berkovich tip (half angle, 65.27°; included angle, 142.30°). The calibration of nanoindentation was performed using a standard sapphire before each test. Each test consisted of a 5 s loading to 10 mN, followed by a 2 s holding and a 5 s unloading. The corresponding loading force and pressed depth of each sample were recorded to calculate hardness and modulus using Oliver–Pharr method[51]. Elastic recovery was calculated to evaluate material resilience[43]. It should be noted that the coating samples for nanoindentation measurement were coated quartz glass with a coating thickness of 200 μm to eliminate the effect of substrate.

Rheological test
Rheological test was performed on a rheometer (MCR-302, Anton-Paar, Austria) utilizing a 25 mm diameter parallel steel plate with the frequency of 1 Hz.

Fourier transform infrared spectroscopy
FTIR spectra were acquired with a Nicolet 6700 spectrometer (Nicolet, America) in transmission mode with 32 scans ranging from 4000 to 650 cm^{-1} at a resolution of 4 cm^{-1}. Samples were mixed with dry KBr and pressed into plates for measurement.

Solid NMR spectra
^{19}F and ^{29}Si CP-MAS NMR spectra were obtained with an Agilent 600 M NMR spectrometer.

External electrostatic charges decay
Each sample was left on a grounded substrate to discharge for at least 24 h under an argon atmosphere. Electroneutrality was confirmed by measuring net charge density (< ± 0.005 nC cm^{-2}). After these treatments, samples were charged by five shots (~1.5 nC cm^{-2}) from an ion gun (Zerostat, Sigma Aldrich). Positive and negative ions and/or charges were generated by pulling and releasing the trigger of ion guns, respectively. Surface charge densities of samples versus time were measured under ambient conditions (room temperature, ~25 °C; relative humidity, ~40%) using a Model 284 Faraday cup & cage (Monroe Electronics, America) connected to the 6514B electrometer. Precautions were taken to minimize external disturbances, including washing gloves and tweezers with ethanol before the experiments and wearing an electrostatic bracelet.

Kelvin probe force microscopy
Surface potential images of different samples before and after abrasion with a copper rod were recorded at room temperature under dry nitrogen atmosphere on a Dimension Icon (Bruker, America) in KPFM mode. The utilized probe was MESP-V2 with a spring constant of 3.0 N m^{-1} and conductive coating of CoCr. Each sample was left on a grounded substrate to discharge for at least 24 h under argon atmosphere, and their electroneutrality was further confirmed by measuring net charge density (< ± 0.005 nC cm^{-2}). All images were analyzed by NanoScope Analysis version 2.0.

Atomic force microscope
AFM height and phase images were recorded under ambient conditions (room temperature, ~25 °C; relative humidity, ~40%) on a Dimension Icon (Bruker, America) in tapping mode. The utilized probe was TESPA-V2 with a spring constant of 42 N m^{-1} and back side coating of reflective Al. All images were analyzed by NanoScope Analysis version 2.0.

Refractive index
Refractive index spectra of samples were obtained on a IR-VASE Mark II M-2000UI instrument (J.A.Woollam, America) with a wavelength range of 250–1600 nm. To acquire accurate results, coating and CPI films were with a thickness of 30 μm.

Ultraviolet-visible Spectroscopy
Ultraviolet-visible (UV-Vis) spectra of samples were measured on a UV − 3600 UV-Vis spectrophotometer (Shimadzu, Japan) with a wavelength range of 200–800 nm. Samples used for transmittance tests were CPI films with a thickness of 50 μm and FTD-coated CPI films (both the CPI films and coating had a thickness of 50 μm), with air as the baseline. Samples used for transmittance tests of the FTD coating were FTD-coated quartz glass (with a coating thickness of 50 μm and quartz glass thickness of 2 mm) after removing the glass substrate baseline. Reflectance from 200 to 800 nm for CPI films and FTD-coated CPI films were recorded on a Lambda 750 s UV-Vis spectrophotometer (Perkin Elmer, America).

Contact angle
The contact angle was obtained under ambient conditions (room temperature, ~25 °C; relative humidity, ~40%) on a DSA25 instrument (KRUSS, Germany). Contact angles of water and diiodomethane were used to calculate the surface energies of samples by using Owens-Wendt-Rabel-Kaelble (OWRK) method[52]. Droplets of 2 μL were utilized for tests, and each test was repeated at least 3 times in different areas on a sample. It should be noted that UTG used for contact angles measurement was rinsed three times with dichloromethane and ethanol, then dried with nitrogen before testing for eliminating the transfer of a small quantity of release agents (silicone oils) from the plastic protective films onto the UTG surface.

Pencil hardness
Pencil hardness results were obtained under ambient conditions (room temperature, ~25 °C; relative humidity, ~40%) on an Elecometer 501 pencil hardness instrument following ASTM D3363 protocol. Standard pencils (Mitsubishi, Japan) with hardness ranging from 6B (the softest), 5 ~ 1B, HB, F, 1 ~ 8H, to 9H (the hardest) were held against the surface of samples with an angle of 45° and then pushed away. The pencil hardness results of samples were evaluated by the hardest pencil that could not damage the surface of samples in at least five different areas. The load weight was 0.75 kg.

Scratch resistance
Scratch resistance tests were conducted under ambient conditions (room temperature, ~25 °C; relative humidity, ~40%) on a ZOT-6014

339 abrasion test machine (Guangdong Zhongtian Instrument Co., Ltd, China). Fresh steelwool (grade #0000, fiber width is 25 μm) was wrapped and firmly fixed on the tester for each scratch resistance characterization. The vertical contact pressure was ~ 50 kPa (the contact area was ~ 1 cm^2, and the load was ~ 500 g), and the abrasion frequency was 1 Hz.

Friction coefficient

The friction coefficients were determined from nano-scratch results under ambient conditions (room temperature, ~25 °C; relative humidity, ~40%) using a TI 980 nanoindenter (Bruker, USA). The load and nano–scratching distance were 500 μN and 15;μm, respectively.

Flexibility

Flexibility was evaluated by testing the sample's r_c in cyclic bending tests. The FTD–coated CPI films (the thickness of both CPI films and coating was 50 μm) were repeatedly bent into a U–shape and recovered to flat about 10,000 times under ambient conditions (room temperature, ~25 °C; relative humidity, ~40%) using a homemade continuous bending apparatus. There were no cracks in the bending areas over 10,000 cycles of bending when the r_c was set to 1.5 mm. However, when the r_c was reduced to 1.0 mm, cracks were generated after 300 cycles of bending.

Adhesion strength

The adhesion strength of FTD coating on CPI films was performed on a PosiTest AT–A automatic pull–off adhesion tester (DeFelsko, America) under ambient conditions (room temperature, ~25 °C; relative humidity, ~40%) in accordance with ASTM D4541. The aluminum spindles with a diameter of 20 mm were tightly adhered onto the coating surface using glue. The pull speed was 0.2 MPa s^{-1}. The result was obtained from 3 times parallel tests.

Touch test

A CPI film coated with FTD coating was pasted on half of the touch panel, and shots from an ion gun were applied to the touch panel with and/or without CPI film coated with FTD coating before the touch test. Touch test results were evaluated based on the writing effect of "SCU". It should be noted that touch panels used for the touch test were eliminated electrostatic modules by cellphone repair shops.

Statistical analysis

In this study, every statistical result was conducted using data obtained from three parallel samples, with each experiment repeated at least three times. The statistical data presented includes means ± standard deviations, or in some cases, means incorporating all results. Mean and STDEV.P functions within Microsoft Excel software were employed to calculate the means and standard deviations, respectively.

Data availability

The authors declare that the data supporting the findings of this study are available within the article and Supplementary Information. Additional datasets related to this study are available from the corresponding authors upon request. Source data are provided with this paper.

References

1. Albinsson, P.–A. & Zhai, S. High precision touch screen interaction. *Proceedings of the SIGCHI conference on Human factors in computing systems*, 105–112 (2003).
2. Kim, C. –C., Lee, H. –H., Oh, K. H. & Sun, J. –Y. Highly stretchable, transparent ionic touch panel. *Science* **353**, 682–687 (2016).
3. Shi, X. et al. Large–area display textiles integrated with functional systems. *Nature* **591**, 240–245 (2021).
4. Heng, W., Solomon, S. & Gao, W. Flexible electronics and devices as human–machine interfaces for medical robotics. *Adv. Mater.* **34**, 2107902 (2022).
5. Choi, H. W. et al. Smart textile lighting/display system with multifunctional fibre devices for large scale smart home and IoT applications. *Nat. Commun.* **13**, 814 (2022).
6. Groenendaal, L. B. Conductive polymers. In *Flexible Flat Panel Displays*, 135–161 (Wiley, 2005).
7. Zhang, W. et al. ESD mechanism research of capacitive touch display module. In *SID Symposium Digest of Technical Papers*, 1017–1019 (Wiley, 2019).
8. Kim, M. et al. Transparent, water–repellent, antiviral, antistatic, and flexible Cu–plasma–polymerized fluorocarbon nanocomposite thin films. *ACS Appl. Mater. Interfaces* **13**, 10301–10312 (2021).
9. Crawford, G. P. Flexible flat panel display technology. In *Flexible Flat Panel Displays*, 1–9 (Wiley, 2005).
10. Choi, G. M. et al. Flexible hard coating: glass-like wear resistant, yet plastic–like compliant, transparent protective coating for foldable displays. *Adv. Mater.* **29**, 1700205 (2017).
11. Zhang, K., Huang, S., Wang, J. & Liu, G. Transparent omniphobic coating with glass–like wear resistance and polymer–like bendability. *Angew. Chem., Int. Ed.* **58**, 12004–12009 (2019).
12. Samy, M. M., Mohamed, M. G. & Kuo, S. –W. Pyrene–functionalized tetraphenylethylene polybenzoxazine for dispersing single-walled carbon nanotubes and energy storage. *Compos. Sci. Technol.* **199**, 108360 (2020).
13. Liang, Y. et al. Biomimetic underwater self–perceptive actuating soft system based on highly compliant, morphable and conductive sandwiched thin films. *Nano Energy* **81**, 105617 (2021).
14. Matsuhisa, N. et al. Printable elastic conductors with a high conductivity for electronic textile applications. *Nat. Commun.* **6**, 7461 (2015).
15. Hong, S. et al. Nonvacuum, maskless fabrication of a flexible metal grid transparent conductor by low-temperature selective laser sintering of nanoparticle ink. *ACS Nano* **7**, 5024–5031 (2013).
16. Wang, N., Yang, X. & Zhang, X. Ultrarobust subzero healable materials enabled by polyphenol nano–assemblies. *Nat. Commun.* **14**, 814 (2023).
17. Hong, C., Li, B., Zhang, J., Li, Y. & Sun, J. Supramolecular polymer–based Ionogels enable large-scale fabrication of stable smart windows with room–temperature closed–loop recyclability and self–healing capability. *Adv. Funct. Mater.* **34**, 2313781 (2024).
18. Fox, J. et al. High–strength, healable, supramolecular polymer nanocomposites. *J. Am. Chem. Soc.* **134**, 5362–5368 (2012).
19. Li, Y., Chen, S., Li, X., Wu, M. & Sun, J. Highly transparent, nanofiller–reinforced scratch-resistant polymeric composite films capable of healing scratches. *ACS Nano* **9**, 10055–10065 (2015).
20. Ritchie, R. O. The conflicts between strength and toughness. *Nat. Mater.* **10**, 817–822 (2011).
21. Chen, R. et al. Transparent polymer–ceramic hybrid antifouling coating with superior mechanical properties. *Adv. Funct. Mater.* **31**, 2011145 (2021).
22. Zhang, Y. et al. Multifunctional hard yet flexible coatings fabricated using a universal step–by–step strategy. *Adv. Sci.* **9**, 2200268 (2022).
23. Zhu, J. et al. Facile fabricated transparent anti-smudge coating with high hardness and excellent flexibility from MTQ and branched silicone resins. *Prog. Org. Coat.* **185**, 107907 (2023).
24. Kim, Y. H. et al. Transparent urethane–siloxane hybrid materials for flexible cover windows with ceramic-like strength, yet polymer–like modulus. *ACS Appl. Mater. Interfaces* **10**, 43122–43130 (2018).
25. Lin, X. et al. Engineering the properties of transparent hybrid coating toward high hardness, excellent flexibility, and multifunction. *ACS Appl. Mater. Interfaces* **14**, 39432–39440 (2022).

26. Zhang, P., Qin, B. & Xia, J. UV curable robust durable hydrophobic coating based on epoxy polyhedral oligomeric silsesquioxanes (EP–POSS) and their derivatives. *ACS Omega* **7**, 17108–17118 (2022).
27. Lin, X. et al. Topology–enabled simultaneous enhancement of mechanical and healable properties in glassy polymeric materials using larger POSS. *Chem. Mater.* **36**, 575–584 (2023).
28. Pan, K. et al. Flexible transparent hydrophobic coating films with excellent scratch resistance using Si-doped carbonized polymer dots as building blocks. *ACS Appl. Mater. Interfaces* **15**, 26060–26068 (2023).
29. Hou, Y. et al. Superior hard but quickly reversible Si–O–Si network enables scalable fabrication of transparent, self–healing, robust, and programmable multifunctional nanocomposite coatings. *J. Am. Chem. Soc.* **144**, 436–445 (2021).
30. Bassindale, A. R., Pourny, M., Taylor, P. G., Hursthouse, M. B. & Light, M. E. Fluoride–ion encapsulation within a silsesquioxane cage. *Angew. Chem., Int. Ed.* **42**, 3488–3490 (2003).
31. Anderson, S. E. et al. Structural investigation of encapsulated fluoride in polyhedral oligomeric silsesquioxane cages using ion mobility mass spectrometry and molecular mechanics. *Chem. Mater.* **20**, 4299–4309 (2008).
32. Deng, Y. –Y. et al. Fluoride ion encapsulated polyhedral oligomeric silsesquioxane: A novel filler for polymer nanocomposites with enhanced dielectric constant and reduced dielectric loss. *Compos. Sci. Technol.* **189**, 108035 (2020).
33. Laird, M. et al. Post-synthesis modification of functionalised polyhedral oligomeric silsesquioxanes with encapsulated fluoride–enhancing reactivity of T_8–F POSS for materials synthesis. *New J. Chem.* **45**, 4227–4235 (2021).
34. Bureš, F. Quaternary ammonium compounds: simple in structure, complex in application. *Top. Curr. Chem.* **377**, 14 (2019).
35. Owen, M. J. Surface tension of polytrifluoropropylmethylsiloxane. *J. Appl. Polym. Sci.* **35**, 895–901 (1988).
36. Owen, M. J. Poly[methyl(3,3,3–trifluoropropyl)siloxane]. In *Handbook of Fluoropolymer Science*, 183–200 (Wiley, 2014).
37. Wang, D. et al. Design of robust superhydrophobic surfaces. *Nature* **582**, 55–59 (2020).
38. Ge, Q. & Liu, H. Rational design and preparation of superhydrophobic photo-cured hybrid epoxy coating modified by fluorocarbon substituted silsesquioxane–based nanoparticles. *Prog. Org. Coat.* **172**, 107089 (2022).
39. Si, G. & Chen, C. Cyclic–acyclic monomers metathesis polymerization for the synthesis of degradable thermosets, thermoplastics and elastomers. *Nat. Synth.* **1**, 956–966 (2022).
40. Wannasiri, C., Chanmungkalakul, S., Bureerug, T., Sukwattanasinitt, M. & Ervithayasuporn, V. Ultrafast synthesis of silicone elastomers using silsesquioxane cages as crosslinkers. *Chem. Commun.* **59**, 5471–5474 (2023).
41. Mohamed, M. G. et al. Ultrastable porous organic/inorganic polymers based on polyhedral oligomeric silsesquioxane (POSS) hybrids exhibiting high performance for thermal property and energy storage. *Micropor. Mesopor. Mater.* **328**, 111505 (2021).
42. Sun, R. et al. Flexible cyclosiloxane–linked fluorescent porous polymers for multifunctional chemical sensors. *ACS Macro Lett* **9**, 43–48 (2019).
43. Musil, J. Flexible hard nanocomposite coatings. *RSC Adv* **5**, 60482–60495 (2015).
44. Fang, W. et al. Organic–inorganic covalent–ionic molecules for elastic ceramic plastic. *Nature* **619**, 293–299 (2023).
45. Rahimi, A. & García, J. M. Chemical recycling of waste plastics for new materials production. *Nat. Rev. Chem.* **1**, 0046 (2017).
46. Li, Z. et al. Healable and recyclable elastomers with record–high mechanical robustness, unprecedented crack tolerance, and superhigh elastic restorability. *Adv. Mater.* **33**, 2101498 (2021).
47. Zheng, N., Xu, Y., Zhao, Q. & Xie, T. Dynamic covalent polymer networks: a molecular platform for designing functions beyond chemical recycling and self–healing. *Chem. Rev.* **121**, 1716–1745 (2021).
48. Liu, Z. et al. Chemical upcycling of commodity thermoset polyurethane foams towards high–performance 3D photo–printing resins. *Nat. Chem.* **15**, 1773–1779 (2023).
49. Sun, F. et al. Vascular smooth muscle–inspired architecture enables soft yet tough self–healing materials for durable capacitive strain–sensor. *Nat. Commun.* **14**, 130 (2023).
50. Wang, W. et al. Mechanically robust reversibly cross-linked polymers with closed–loop recyclability for use in flexible printed circuit boards. *Adv. Funct. Mater.* **34**, 2401822 (2024).
51. Oliver, W. C. & Pharr, G. M. An improved technique for determining hardness and elastic modulus using load and displacement sensing indentation experiments. *J. Mater. Res.* **7**, 1564–1583 (1992).
52. Owens, D. K. & Wendt, R. Estimation of the surface free energy of polymers. *J. Appl. Polym. Sci.* **13**, 1741–1747 (1969).

Acknowledgements

The authors acknowledge support from the National Natural Science Foundation of China (52103317 to S.–R.F. and 22475139 to D.H.) and State Key Laboratory of Polymer Materials Engineering (sklpme2023–2–05 to D.H.).

Author contributions

X.L. was associated with conceptualization, investigation, experiments, formal analysis, writing–original draft, review & editing, methodology, and resources. C.–Y.L. and L.–X.L. were associated with experiments. Q.–Y.G. was associated with writing–review & editing and methodology. Y.Z. was associated with methodology. S.–R.F. was associated with funding acquisition and writing–review & editing. Q.Z., and F.C. were associated with writing–review & editing. D.H. was associated with conceptualization, investigation, formal analysis, funding acquisition, writing–review & editing, methodology, resources, and project administration supervision. Q.F. was associated with formal analysis, writing–review & editing, resources, and project administration supervision.

Competing interests

The authors declare no competing interests.

Additional information

Supplementary information The online version contains supplementary material available at https://doi.org/10.1038/s41467-024-54083-7.

Correspondence and requests for materials should be addressed to Di Han or Qiang Fu.

Peer review information *Nature Communications* thanks Byeong-Soo Bae, Sang-Jin Lee and the other anonymous reviewer(s) for their contribution to the peer review of this work. A peer review file is available.